

Steering device-quality perovskites with unique substrate tolerance

Ningyu Ren

Inner Mongolia University/Nankai University

Pengyang Wang

Nankai University

Junke Jiang

Eindhoven University of Technology <https://orcid.org/0000-0003-2962-766X>

Renjie Li

Nankai University

Wei Han

Nankai University

Jingjing Liu

Nankai University

Zhao Zhu

Nankai University

Bingbing Chen

Nankai University

Qiaojing Xu

Nankai University

Tiantian Li

Inner Mongolia University

Biao Shi

Nankai University

Qian Huang

Institute of Photo Electronics Thin Film Devices and Technology

Dekun Zhang

Institute of Photo Electronics Thin Film Devices and Technology

Sofia Aperi

Eindhoven University

Geert Brocks

Computational Materials Science, Faculty of Science and Technology and MESA+ Institute for Nanotechnology, University of Twente, 7500 AE Enschede, the Netherlands.

Chenjun Zhu

Inner Mongolia University

Shuxia Tao

Eindhoven University of Technology <https://orcid.org/0000-0002-3658-8497>

Ying Zhao

Institute of Photo Electronics Thin Film Devices and Technology

Xiaodan Zhang (✉ xdzhang@nankai.edu.cn)

Nankai University

Article

Keywords:

Posted Date: January 26th, 2022

DOI: <https://doi.org/10.21203/rs.3.rs-1153958/v1>

License:  This work is licensed under a Creative Commons Attribution 4.0 International License.

[Read Full License](#)

Abstract

Polycrystalline perovskite films fabricated on flexible and textured substrates often are highly defective, leading to poor performance of perovskite devices. Finding substrate-tolerant perovskite fabrication strategies is therefore paramount. Herein, we show that a small amount of Cadmium Acetate (CdAc₂) in PbI₂ precursor solution results in nano-hole array films and improves the diffusion of organic salts in PbI₂, and promotes favorable crystal orientation and suppresses non-radiative recombination.

Polycrystalline perovskite films on flexible substrate with ultra-long carrier lifetimes exceeding 6 μ s are achieved. Eventually, a record PCE of 22.78% is obtained for single-junction flexible perovskite solar cells (FPSCs). Furthermore, we find this strategy is also demonstrated to be applicable for textured tandem solar cells. Our perovskite/silicon tandem solar cells (TSCs) with CdAc₂ showed an efficiency of 29.25% (0.5003 cm²), with a certified value being 23.07% (11.8792 cm²), respectively, the highest value reported for solution-based TSCs. Un-encapsulated TSCs based on CdAc₂ maintain 109.78% of their initial efficiency after operation at maximum power point under continuous one-sun illumination for 300 hours at 45 oC in N₂ atmosphere. This strategy will provide facile access to high-efficiency perovskite-based solar cells.

Full Text

Metal halide perovskite solar cells (PSCs) are a promising competitor to traditional silicon photovoltaics, with their power conversion efficiency (PCE) already exceeding 25%¹⁻³. The lightweight perovskite thin films are especially suitable for flexible devices, which are applicable in novel fields, such as vehicle-integrated photovoltaics, aerial vehicles, and other stretchable electronics applications⁴⁻¹⁰. Although in a very short time, there is a rapid increase in the PCE of flexible perovskite solar cells (FPSCs) from 2.62% to 21.73%^{11,12}, the performance of FPSCs still lies behind that of their rigid counterparts.

The quality of the crystalline perovskite films and thus the performance of FPSCs strongly depends on the flexible substrate^{5,6}, which influences the nucleation density, crystal orientations, and crystal growth rates of the perovskite film⁷. A rough surface means more nucleation sites and faster crystal growth rates, which will result in low coverage of defects-rich perovskite films^{13,14}. Another negative factor can be the thermal expansion coefficient mismatch between perovskite and substrates, which will inevitably form lattice strain, deep level defects, and even cracks in perovskite films during the thermal annealing process^{7,15,16}. The most widespread substrates in FPSCs, polyethylene terephthalate (PET) or polyethylene naphthalate (PEN), suffer from high surface roughness and prominent thermal shrinkage. Therefore it is challenging to obtain high-quality perovskite films on flexible substrates¹⁷⁻¹⁹.

Device-quality crystalline perovskite films usually have a larger grain size²⁰⁻²², which is achieved by delaying nucleation and promoting crystal growth according to the LaMer model²³. Some strategies have been proven to effectively control the nucleation and crystal growth of device-quality crystalline

perovskite films on rigid substrates, including adding additives, such as Cesium (Cs) Bromide (Br-), chloride (Cl-), ionic liquid, thiocyanate (SCN-) anions²⁴⁻²⁸, solvent coordination complexes²⁹, or formate anions (HCOO-)^{30,31} and so on. To improve the efficiency of FPSCs, researchers have made great efforts, including optimizing the flexible substrate, the transport layer material, and preparation process^{8-10,32-34}, using lower preparation temperature^{14,15,35,36}, interface passivation^{37,38} and doping³⁹⁻⁴¹. Up to now, the performance of FPSCs is still not very high.

Flexible substrates are not the only challenging surfaces for the growth of perovskite films. The perovskite/silicon tandem solar cells (TSCs) are promising candidates to surpass the single-junction solar cells efficiency limit⁴²⁻⁴⁵. One of the biggest challenges for enabling the high-efficiency of TSCs is the compatibility of perovskite crystal growth with micron-sized pyramidal textured substrates^{46,47}. Currently, the highest PCE of TSCs based on the textured substrate has reached up to 27.4%⁴⁸, but with rational manipulation of the perovskite crystal growth and passivation of deep level traps, more efficient tandem solar cells can be achieved.

In this work, we introduce Cadmium Acetate (CdAc_2) as a perovskite precursor solution additive to manipulate the perovskite crystal growth, achieving excellent optoelectronic properties on the flexible substrate and textured silicon substrate. Using density functional theory (DFT) calculations, we confirm that CdAc_2 coordinates with lead iodide (PbI_2), forming an intermediate phase and slowing down the perovskite crystal growth rate, which eventually results in a better crystallinity of the final perovskite film. The grain boundaries are also passivated by the crosslinking structure of Ac^- , resulting in the excellent thermal durability of the FAPbI_3 film. As a result, we demonstrate that with the synergistic effect of Cd ion doping and Ac-ion-assisted crystallization, the intrinsic defect density of perovskite polycrystalline thin film is vastly reduced, and the carrier lifetime is increased to over 6 μs . We achieved PCEs of 24.46% and 22.78% for single-junction PSCs on the rigid and flexible substrates. The latter is the highest reported for flexible PSCs to date. We also applied the CdAc_2 in perovskite/silicon tandem solar cells and obtained an efficiency of 29.25% and a certified efficiency of 23.07% with aperture areas of 0.5003 and 11.8792 cm^2 , respectively. Operational stability showed that un-encapsulated TSCs based on CdAc_2 maintain 109.78% of their initial efficiency after continuous one-sun illumination for 300 hours at 45 °C in the N_2 atmosphere.

Formation of nano-hole array PbI_2 and FAPbI_3 films

The FPSCs in this work are based on FAPbI_3 and are fabricated by using a two-step solution method. In the two-step sequential deposition, the quality of the final perovskite films strongly depends on the PbI_2 films. In general, a compact crystalline PbI_2 film tends to form on a flexible substrate. In this work, we developed an effective method to create PbI_2 films with arrays of nano-sized pinholes at step one by introducing CdAc_2 into PbI_2 precursor solution. These pinholes allow for improved diffusion and

intercalation of the organic ammonium cations in the second step of the deposition and finally produce perovskites with large and uniform grains.

To gain insights into how CdAc_2 may influence the microscopic structure of the perovskites, we carried out several density functional theory (DFT) calculations (details in **SI notes 1,2**). Our results show that Cd^{2+} can be incorporated in the PbI_2 lattice, substituting Pb^{2+} , and Ac^- can bind at the surfaces of PbI_2 , replacing I^- . Because Ac^- is a larger and more asymmetric ion, the direct consequence of the latter substitution is an increased distance between the PbI_2 layers and weakened binding between each layer by 0.05 eV/formula unit (Fig. 1a). As shown in supplementary Fig. 1, the introduction of Ac^- leads to a significant decrease in the peak intensity of PbI_2 . This finding suggests that less densely packed PbI_2 films are more likely to form when Ac^- is added to PbI_2 precursor solution, which may stimulate the formation of pinholes.

The presence of pinholes can potentially facilitate the diffusion and intercalation of FAI in the PbI_2 film, where the perovskite is formed, resulting in more uniform perovskite films, as illustrated in Figs. 1b and c. Our calculations show that during the reactions of FAI with Ac^- -doped PbI_2 films the Ac^- is readily replaced by I^- to produce a clean PbI_2 surface. At the next stage, the perovskite formation, the role of the Cd becomes important, as the transformation from a face-sharing structure in PbI_2 to a corner-sharing structure in perovskite requires the breaking of some of the metal-iodine bonds in the MI_2 layer and the formation of new metal-iodine bonds for the 3D perovskite. The Cd incorporated in the PbI_2 lattice structure (in the first step) has direct consequences for the kinetics of the overall transformation. In the Cd-doped PbI_2 structure, creating an I vacancy near a Cd site (to facilitate ion transport) costs 0.02 eV/formula unit more energy than near a Pb site, whereas in the Cd-doped perovskite structure, it costs 0.03 eV/formula unit less energy. This indicates that the incorporation of Cd in the lattice increases the activation barriers for the reaction of converting the layered structure to a 3D perovskite structure. This can lead to a slower crystallization process and result in larger and more uniform perovskites grains.

To further elucidate how CdAc_2 affects the crystallization of the perovskite films, grazing incidence X-ray diffraction (GIXRD) with various X-ray incident angles was employed, as shown in Figs. 1b and c. From the GIXRD, it is found that the crystal orientation is significantly different at the surface and bottom of the perovskite film with CdAc_2 . It is clearly shown that the perovskite film with CdAc_2 exhibits a prominent (111) orientation at the bottom, relative to other crystal planes' peaks, which indicates that the (111) crystals grew faster than differently oriented crystals with the presence of CdAc_2 . The (111) plane orientation is parallel to the substrate and favorable perovskite lattices⁴⁹. Keith P. McKenna⁵⁰ found the (111) plane is extremely stable in pure formamidinium lead iodide and presents relatively small barriers (< 100 meV) to transport carriers⁵¹. Furthermore, the XRD patterns in supplementary Figs. 2 and 3 show that the (111) orientation peak of FAPbI_3 was enhanced with CdAc_2 on both rigid and flexible substrates. The prominent (111) orientation with lower trap density enables efficient PSCs on both rigid and flexible substrates as will be demonstrated in the following.

Enhanced optical and electrical properties of FAPbI₃ films

To gain insight into the properties of our perovskite films, we carried out confocal photoluminescence (PL) mapping measurements to investigate the morphologies and optoelectronic properties of the perovskite films with and without CdAc₂ (Fig. 2a). We observed an enhanced photoluminescence performance with better uniformity and stronger intensity for the perovskite with CdAc₂. As shown in Fig. 2b, the PL peak wavelength distribution of the CdAc₂ treated perovskite film is obviously narrower than the reference one, indicating a more uniform film. Moreover, the CdAc₂-treated perovskite film exhibits higher PL mapping intensity than the control film, showing better optical properties (Fig. 2c). This can also be confirmed by time-resolved photoluminescence (TRPL) measurements (Fig. 2d), in which the CdAc₂-treated perovskite film exhibits a much longer carrier lifetime (6514 ns) than the control film (Supplementary Table S1), underlining the benefit of CdAc₂ on the perovskite film by suppressed non-radiative recombination. To further investigate the charge transfer properties of perovskite films, steady-state PL and absorption spectra were also conducted. As shown in Fig. 2e, the emission intensity of the perovskite film is enhanced dramatically with the incorporation of CdAc₂, indicating a decrease of non-radiative recombination, consistent with PL mapping and TRPL results. The ultraviolet-visible (UV-Vis) absorption spectra are slightly enhanced. We attribute this to the larger grain size and the decreased defect density.

The low defect density can be explained by two factors: (i) the better intercalation of FAI in the pinhole-rich PbI₂ films in the first step and slower crystallization (effect of Cd⁺) in the second step have overall led to large and high-quality perovskites and (ii) the Ac⁻ species on the grain boundaries passivate the undercoordinated Pb²⁺, preventing further degradation, i.e. the formation and diffusion of I vacancy defects. Such passivation effect is verified by additional DFT calculations, where the relative binding strength of Ac⁻ (compared to I⁻) to Pb is calculated by moving the target anion on the PbI₂-terminated surface away at a distance of ~4 Å (Supplementary Fig. 4). The energies show that Ac⁻ has high binding energy equally to recently reported HCOO⁻², and is about 1 eV higher than that of I⁻ (Supplementary Fig. 5).

To further investigate the influence of the CdAc₂ on the properties of perovskite film, we carried out the X-ray Photoelectron Spectroscopy (XPS). In the Pb 4f spectra of both perovskite films (Fig. 2f), we can observe two additional peaks (located at 136.4 and 141.3 eV) for the control perovskite film, which correspond to metallic lead and originate from the unintended losses of iodine, leading to deep-level defects and non-radiative recombination. Fortunately, it seems that the formation of metallic Pb can be suppressed by the addition of CdAc₂. Besides, it can be estimated from Fig. 2f and supplementary Fig. 6 that the ratio of Pb/I is 1:2.26 and 1:2.63 in the perovskite film without and with CdAc₂ doping, respectively, indicating that the iodine vacancies on the surface of the perovskite film are reduced with the addition of CdAc₂. The metallic lead is widely perceived as contributing to deep-level defects and result in non-radiative recombination, which also can be found in the control perovskite

film from supplementary Fig. 7. The presence of CdAc₂ succeeded in preventing the formation of metallic Pb. We also confirm the effect of CdAc₂ on PbI₂ by ¹³C nuclear magnetic resonance (NMR) spectra (Fig. 2g). With the addition of CdAc₂, the peak of C=O moved from 167.2 ppm to 167.6 ppm, which indicates a strong interaction between CdAc₂ (C=O group) and Pb²⁺. Fig. 2h presents the TGA spectra of the PbI₂ solution and the different adducts. The dimethyl sulfoxide (DMSO) adduct of PbI₂/DMF decomposes rapidly at 80 °C, while PbI₂/DMF-DMSO-CdAc₂ decomposes at 139°C. It indicates that the PbI₂/DMF-DMSO-CdAc₂ is more stable than the PbI₂/DMF-DMSO due to the strong molecular interaction between CdAc₂ and PbI₂.

Photovoltaic performance and stability of flexible perovskite solar cells

Based on the above results, we conducted a series of experiments fabricating rigid and flexible perovskite solar cells with the structure of ITO/SnO₂/Perovskite/Spiro-OMeTAD/Au (Fig. 3a). The FAPbI₃ active layer was deposited by a two-step method, with CdAc₂ added to the precursor solution. The cross-sectional SEM image shows that the thickness of the perovskite absorber layer is about 750-nm with grain throughout the film, indicating high crystallinity (Figs. 3b and c). The element distribution in FPSCs (Supplementary Figs. 8 and 9), indicates that Cd is uniformly distributed in the perovskite film. Combined with the benefits of effectively decreasing the trap density with the addition of CdAc₂ as discussed in the previous section, with the good transmittance of the flexible PET substrate used in this work (Supplementary Fig. 10), we achieved the champion current density voltage (*J-V*) curves of FPSCs. As shown in Fig. 3d, the control FPSCs exhibited a PCE of 19.86% with *J*_{SC} of 24.32 mA/cm², *V*_{OC} of 1.096 V, and fill factor (*FF*) of 74.48% under standard AM1.5 solar illumination. The CdAc₂-treated FPSCs reached the champion PCE of 22.78%, along with a *J*_{SC} of 24.63 mA/cm², *V*_{OC} of 1.167 V, and an *FF* of 79.27%, which is the highest PCE reported for flexible PSCs to date (Supplementary Fig. 3e and Table 2). More details for the statistical photovoltaic performance of FPSCs without passivation are shown in supplementary Fig. 11. Moreover, a steady PCE output of 22.7% was demonstrated by maximum power point (MPP), as shown in supplementary Fig. 12. The corresponding external quantum efficiencies (EQE) of the devices are exhibited in Fig. 3f. The CdAc₂-treated device shows an integrated *J*_{SC} of 24.75 mA/cm², slightly higher than the control device, matching *J-V* curves. The bandgap of the perovskite is 1.53 eV and remains constant regardless of the presence of CdAc₂, as shown in supplementary Fig. 13. A champion PCE of 24.46% was achieved on the rigid substrate by adding CdAc₂, with a *J*_{SC} of 25.75 mA/cm², a *V*_{OC} of 1.169 V, and a fill factor (*FF*) of 81.24% (Supplementary Fig. 14).

To provide more solid evidence on the charge recombination process, we measured the dependence of the *V*_{OC} on the light intensity for the control and CdAc₂-treated FPSCs. The slope deviation of *V*_{OC} versus the natural logarithm of light intensity from *k*BT/*q* indicates the occurrence of non-radiative trap assisted recombination (monomolecular recombination), which has been reported to be a dominant recombination pathway in PSCs. As shown in Fig. 3g, the control FPSCs exhibited a slope of 1.91 *k*BT/*e*, while the CdAc₂-treated FPSCs showed a much smaller slope of 1.32 *k*BT/*e*. This indicates that defect-

assisted non-radiative recombination was effectively suppressed by using CdAc₂, which is in accordance with the enhanced V_{OC} and FF . The lower leakage dark current (Supplementary Fig. 15) also improved charge transport and decreased recombination loss in the CdAc₂-treated FPSCs. To quantify the trap density in perovskite films, we performed space-charge-limited-current (SCLC) of corresponding perovskite films (Fig. 3h). As a result, the perovskite film with CdAc₂ has a smaller VTFL than that of the control film, indicating that films with CdAc₂ can suppress the formation of defects.

To evaluate the carrier transport characteristics and output voltage in FPSCs, capacitance-voltage (C-V) measurements were further performed, and the relevant Mott-Schottky curves were presented in Fig. 3i. The built-in potential (1.166 V) of the CdAc₂-treated FPSCs is extracted to be much larger than that of the control device (1.054 V), which means increased separation of photo-generated carriers and enhanced output voltage of FPSCs. A larger recombination resistance is also beneficial to suppress non-radiative recombination (Supplementary Fig. 16).

Although tremendous progress has been made, long-term stability is still the critical hurdle to commercialization, especially the mechanical performance of FPSCs for their stretchable applications. On that account, we primarily investigated the mechanical stability of un-encapsulated FPSCs with and without CdAc₂ in this study. As depicted in supplementary Fig. 17, after 10000 cycles bend test with a bending radius 3 mm, the performance of FPSCs can still maintain about 80% of the initial value. However, the PCE for the control FPSCs decreased significantly, only providing about 11% of the original PCE after the 1800 cycles bend test. Furthermore, we also conducted cold and hot cycle tests. After 24 cold and hot cycles, the CdAc₂ treated FPSCs provide 87.28% of their initial efficiency, while the control device only maintains 21.59% of its initial efficiency after 13 cold and hot cycles. Based on these results, both bending stability and thermal stability were enhanced by the beneficial effect of the CdAc₂.

Efficient monolithic perovskite/silicon tandem solar cells based on a textured substrate

To further highlight the positive effect of this strategy for perovskite crystallization improvement, we fabricated perovskite/silicon TSCs based on a textured substrate, where the crystal growth would be more complicated than the polished one. The perovskite used here was Cs_{0.22}(FA_{0.76}MA_{0.02})_{0.78}Pb(I_{0.85}Br_{0.15})₃ with a wide bandgap (1.68-eV), which is deposited by one-step method with the addition of CdAc₂. We noticed the quality of wide-bandgap perovskite with CdAc₂ has also been significantly improved from SEM, XRD, and TRPL in supplementary Figs. 18-20. The J - V characteristics and EQE of wide bandgap single-junction PSCs without and with CdAc₂ treatment are shown in supplementary Fig. 21. It is worth mentioning that the pin structure single-junction PSCs shows a high voltage of 1.24 V. The schematic structure of the textured TSCs is shown in Fig. 4a (ITO/HTL/perovskite/C60/SnO₂/IZO/Ag/PDMS), among which ITO (20 nm) served as a recombination layer. The polydimethylsiloxane (PDMS) as light management antireflective foils with excellent optical properties was used in this structure⁵². Figs. 4b and c show the SEM top-view images of the perovskite films based on textured silicon with and without CdAc₂, both of them offer a compact film

and full coverage on the textured silicon wafer (Fig. 4d). But the CdAc₂ treated perovskite film exhibits a much larger grain size. Fig. 4e shows the *J-V* characteristic of the champion perovskite/silicon TSCs with 29.25%, which is the highest efficiency reported for perovskite/silicon TSCs based on textured silicon by spin-coating method (Supplementary Table 3). The statistics of the PCE of TSCs without and with CdAc₂ demonstrated that the CdAc₂-based TSCs are more reproducible and have a higher *V_{oc}* and *FF* (Supplementary Fig. 22). In Fig. 4f, the EQE of the tandem device is presented. The extracted current density of the top and bottom cells are 20.05 mA/cm² and 19.85 mA/cm², respectively, which match well with *J-V* curve. In addition, a large-area perovskite/silicon TSC of the same design with an active area of 11.8792 cm² was successfully fabricated. A PCE of 23.23% was achieved with the CdAc₂ device (Certified with a PCE of 23.07% in supplementary Fig. 23 and Table 4), whereas that of the control device was 19.05% in Fig. 4g. We also examined the long-term operational stability of un-encapsulated TSCs with CdAc₂, which was evaluated under one sun continuous irradiation at maximum power point (MPP) tracking in the N₂ atmosphere. As shown in Fig. 4h, the CdAc₂ treated TSCs maintain 109.78% of the initial efficiency after 300 h. We ascribe the high stability of the TSCs to two main reasons: i) the substitution of Cd indeed slow down the crystallization rate and suppresses the formation of I vacancy and phase segregation⁵³. ii) Moreover, as discussed earlier that our DFT calculations show that the Ac anions coordinate strongly with Pb²⁺ and passivates I vacancy on the grain boundaries of the perovskite films. This evident coordination may also help slow down the perovskite growth process, thus resulting in a larger grain size of the perovskite film with much less trap density in TSCs.

Conclusion

In summary, we have demonstrated a simple and effective approach by using the multifunctional additive CdAc₂ to obtain high-performance FPSCs and TSCs. The strong interactions between CdAc₂ and perovskite components could slow down the grain growth rate, facilitating the growth of device-quality perovskite films with larger grain size, preferred orientation, reduced defects density, and superior electronic properties. Meanwhile, the residual Ac in the perovskite films can passivate ionic defects and act as a molecular lock to prevent thermal degradation. Finally, the residual Ac⁻ in the final perovskite films can also passivate I vacancy defects and act as a molecular lock to prevent thermal degradation. As a result, we achieved a champion PCE of 22.78% based on a flexible substrate, with excellent thermal and mechanical stability. An enhanced PCE of 29.25% can be obtained on textured perovskite/silicon TSCs. We also achieved a certified efficiency of TSCs of 23.07% on large area 11.8792 cm². The CdAc₂ treated TSCs exhibited super stability and retained 109.78% of their initial efficiency under one sun continuous irradiation for 300 hours in an N₂ atmosphere without encapsulation. This work paves the way for the large-scale fabrication of stable and flexible perovskite solar cells.

Methods

Materials. All materials were purchased from either Sigma-Aldrich or Alfa Aesar and used without further purification unless otherwise stated.

FPSCs device fabrication. The pre-patterned ITO-coated PET substrates were cleaned by ultra-sonication with detergent, deionized water, acetone, and isopropanol sequentially, then dried with N_2 . After that, the ITO substrates were treated by UV zone for 20 min. A 20-nm-thick SnO_2 electron transport layer was coated on ITO substrate by spinning at 4000 r.p.m. for 30 s and annealed in the air for 30 min on a hot plate at 130 °C. 1.3 M of PbI_2 in (DMF: DMSO = 9:1) (certain concentrations of CdAc were added to the PbI_2 solutions) was spin-coated on SnO_2 at 1500 r.p.m. for 30 s and then annealed at 70 °C for 1 min. After cooling down to room temperature, the mixture solution of FAI: MAI: MACl (90 mg: 4.5 mg: 9 mg in 1 mL IPA) was spin-coated on PbI_2 at different rotational speeds at 1500 r.p.m. for 30 s. Then the films were annealed at 150 °C for 20 min under ambient air conditions. The hole transport layer by spin coating at a rate of 4000 r.p.m. for 30 s was deposited on top of the perovskite layer by using 2,2',7,7'-tetrakis (*N,N*-di-*p*-methoxyphenylamine)-9,9'-spirobifluorene (Spiro-OMeTAD) solution, which consisted of 72.3 mg Spiro-OMeTAD, 35 μ L bis(trifluoromethane) sulfonamide lithium salt (Li-TFSI) stock solution (260 mg Li-TFSI in 1 mL acetonitrile), 30 μ L 4-tertbutylpyridine, and 1 mL chlorobenzene by spin-coating at 4000 r.p.m. for 30 s. Finally, an 80 nm gold electrode was thermally evaporated. To reduce incident light reflection, anti-reflection film was attached on top of tandem solar cells.

Fabrication and characterization of perovskite/textured silicon tandem solar cells. Silicon heterojunction (SHJ) bottom cells were fabricated on float-zone double-side textured n-doped wafers. The ITO recombination junction (20 nm) was sputtered. Nanocrystalline NiOx (20 nm) is deposited by DC sputtering as the HTL on top of the recombination junction. The perovskite layer was deposited using the single-junction device deposition recipe, except a 1.82 M of the solution was spin-coated on the textured surface. 70 mL of perovskite precursor solution was dropped on top of Si substrate and deposited by one consecutive spin-coating step of 5,000 rpm for 50 s, respectively. During the spin-coating step, 150 mL solvent of ethyl acetate was quickly poured onto the substrate after 20 s. The perovskite-deposited films were annealed on a hotplate at 100 °C for 15 min and 130 °C for 15 min. 20 nm of C60 was thermally evaporated on top of the perovskite layer. The SnO_2 buffer layer (25 nm) was deposited by the thermal atomic layer deposition (ALD) technique. Tetrakis(dimethylamino)tin (TDMASn) and H_2O_2 were used as precursors for the ALD deposition at 100 °C and with 200 cycles. 85 nm of IZO top electrode (50 ohm/sq) was sputtered on the buffer layer with RF power of 30 W over a 2-inch target (90% In_2O_3 /10% ZnO, 99.9% Plasmaterials). The top Ag and bottom Ag/Al contacts were evaporated through a shadow mask using an Angstrom thermal evaporator. Finally, PDMS antireflection films were added to complete the device.

Device characterizations. Scanning electron microscopy results were obtained using field emission scanning electron microscopy (SEM) (Jeol JSM-6700F). The transmittance, reflectance, and absorbance were characterized with a UV-vis-NIR spectrophotometer (Cary 5000, VARIAN). The surface AFM and KPFM were carried out using an ICON2-SYS. The charge transfer kinetics of perovskite films were measured by steady-state photoluminescence (PL) and time-resolved PL (TRPL) with the laser

wavelength of 475 nm and power of 0.2 mW, respectively (Edinburgh FS5). X-ray photoelectron spectroscopy (XPS) and ultraviolet photoelectron spectroscopy (UPS) data were obtained by a multifunctional photoelectron spectrometer (Escalab 250Xi, U.K.). The external quantum efficiency (EQE) was acquired in the direct current mode on the QE system (QE10, Photovoltaic Measurement Co., Ltd.) without any voltage deviation. For tandem devices, the light was biased by infrared (850 nm) and blue (400 nm) light-emitting diodes to saturate the subcells, respectively. *J-V* characteristics of inverted perovskite photovoltaics were measured under 100 mW/cm² light illumination (AM 1.5G) using Keithley 2400 system. The scanning rate in both reverse (from 1.2 V to -0.2 V) and forward (from -0.2 V to 1.2 V) directions were 0.1 V/s, and the scanning step was 0.02 V. During the measurement. The active areas are 8.885 mm², 0.5003 cm², and 11.8792 cm² for flexible single-junction PSCs, small area, and large area tandem solar cells, respectively. The active area is ensured by masks.

Density Functional Theory Calculation. DFT calculations were performed using the Projector Augmented Wave (PAW)^{54,55} method as implemented in the Vienna Ab-Initio Simulation Package (VASP)^{56,57}. The electronic exchange-correlation interaction was described by Perdew, Burke, and Ernzerhof (PBE) functional within the generalized gradient approximation (GGA)⁵⁸ with exchange-correlation functional with Grimme D3 dispersion corrections⁵⁹. Energy and force convergence criteria of 10⁻⁵ eV and 0.02 eV Å⁻¹, respectively, were used in all calculations. The outermost I 5s, 5p; N and C 2s, 2p; H 1s; Pb 6s, 6p, 5d electrons were explicitly treated as valence electrons whose interactions with the remaining ions were modeled by pseudopotentials generated within the projector-augmented wave (PAW) method. The energy cutoff for the plane-wave basis set was set to 500 eV for all calculations. A 2×2×1 *k*-point mesh generated by the Monkhorst-Pack scheme was used for the geometry optimization for all slab models. For the calculation of the defect formation energy of Cd incorporated FAPbI₃, a 5-layer slab was used with a 2×2 cubic supercell and a vacuum region of 20 Å for both the FAI- and PbI₂-terminated surface. Only the top three layers were allowed to relax. The calculated lattice parameter of PbI₂ layer were 4.56 Å, which agree well with the experimental values⁶⁰.

Declarations

Data availability

The data that support the findings of this study are available from the corresponding author upon reasonable request.

Acknowledgments

The authors are grateful to acknowledge the financial support of the National Key Research and Development Program of China (Grant No. 2018YFB1500103), the National Natural Science Foundation of China (Grant No. 61674084, 11564027), the Overseas Expertise Introduction Project for Discipline Innovation of Higher Education of China (Grant No. B16027), Tianjin Science and Technology Project (Grant No. 18ZXJMTG00220). The Key R&D Program of Hebei Province (No. 19214301D), Natural

Science Foundation of Tianjin (No. 20JCQNJC02070), China Postdoctoral Science Foundation (No. 2020T130317), and the Fundamental Research Funds for the Central Universities, Nankai University. The work done in the Netherlands was supported by funding from NWO START-UP and Computational Sciences for Energy Research (CSER) tenure track program of Shell and NWO (Project No. 15CST04-2).

Conflict of Interest

The authors declare no competing interests.

References

1. Kim, G. *et al.* Impact of strain relaxation on performance of *a*-formamidinium lead iodide perovskite solar cells. *Science* **370**, 108–112 (2020).
2. Jeong, J. *et al.* Pseudo-halide anion engineering for α -FAPb₃ perovskite solar cells. *Nature* **592**, 381–385 (2021).
3. Min, H. *et al.* Perovskite solar cells with atomically coherent interlayers on SnO₂ electrodes. *Nature* **598**, 444–450 (2021).
4. Hu, Y. Z. *et al.* Flexible perovskite solar cells with high power-per-weight: progress, application, and perspectives. *ACS Energy Lett.* **6**, 2917–2943 (2021).
5. Hashemi, S. A. *et al.* Recent progress in flexible-wearable solar cells for self-powered electronic devices. *Energy Environ. Sci.* **13**, 685–743 (2020).
6. Lei, Y. H. *et al.* A fabrication process for flexible single-crystal perovskite devices. *Nature* **583**, 790–795 (2020).
7. Meng, X. C. *et al.* Bio-inspired vertebral design for scalable and flexible perovskite solar cells. *Nat. Commun.* **11**, 3016 (2020).
8. Ru, P. B. *et al.* High Electron affinity enables fast hole extraction for efficient flexible inverted perovskite solar cells. *Adv. Energy Mater.* **10**, 1903487 (2020).
9. Chung, J. *et al.* Record-efficiency flexible perovskite solar cell and module enabled by a porous-planar structure as an electron transport layer. *Energy Environ. Sci.* **13**, 4854–4861 (2020).
10. Kim, Y. Y. *et al.* Roll-to-roll gravure-printed flexible perovskite solar cells using eco-friendly antisolvent bathing with wide processing window. *Nat. Commun.* **11**, 5146 (2020)
11. Kumar, M. H. *et al.* Flexible, low-temperature, solution processed ZnO-based perovskite solid state solar cells. *Chem Commun. (Camb)* **49**, 11089–11091 (2013).
12. Wu, S. F. *et al.* Low-bandgap organic bulk-heterojunction enabled efficient and flexible perovskite solar cells. *Adv. Mater.* 2105539 (2021).
13. Heo, J. H. *et al.* Super-flexible bis(trifluoromethanesulfonyl)-amide doped graphene transparent conductive electrodes for photo-stable perovskite solar cells. *J. Mater. Chem. A* **6**, 8251–8258 (2018).

14. Wang, C. L. *et al.* Water vapor treatment of low-temperature deposited SnO₂ electron selective layers for efficient flexible perovskite solar cells. *ACS Energy Lett.* **2**, 2118–2124 (2017).
15. Jiang, J. *et al.* High-performance flexible perovskite solar cells with effective interfacial optimization processed at low temperatures. *ChemSusChem* **11**, 4131–4138 (2018).
16. Jung, J. W. *et al.* Low-temperature processed high-performance flexible perovskite solar cells via rationally optimized solvent washing treatments. *RSC Adv.* **4**, 62971–62977 (2014).
17. Saianand, G. *et al.* Current advancements on charge selective contact interfacial layers and electrodes in flexible hybrid perovskite photovoltaics. *J. Energy Chem.* **54**, 151–173 (2021).
18. Jeong, I. *et al.* A tailored TiO₂ electron selective layer for high-performance flexible perovskite solar cells via low temperature UV process. *Nano Energy* **28**, 380–389 (2016).
19. Huang, K. Q. *et al.* High-performance flexible perovskite solar cells via precise control of electron transport layer. *Adv. Energy Mater.* **9**, 1901419 (2019).
20. Li, N. X. *et al.* Liquid medium annealing for fabricating durable perovskite solar cells with improved reproducibility. *Science* **373**, 561–567 (2021).
21. Lee, J. W. *et al.* A bifunctional lewis base additive for microscopic homogeneity in perovskite solar cells. *Chem* **3**, 290–302 (2017).
22. Watthage, S. C. *et al.* Enhanced grain size, photoluminescence, and photoconversion efficiency with cadmium addition during the two-step growth of CH₃NH₃PbI₃. *ACS Appl. Mater. Interfaces* **9**, 2334–2341 (2017).
23. Liu, C. *et al.* Understanding of perovskite crystal growth and film formation in scalable deposition processes. *Chem. Soc. Rev.* **49**, 1653–1687 (2020).
24. Zhou, Y. *et al.* Metal-doped lead halide perovskites: synthesis, properties, and optoelectronic applications. *Chem. Mater.* **30**, 6589–6613 (2018).
25. Chen, B. *et al.* Grain engineering for perovskite/silicon monolithic tandem solar cells with efficiency of 25.4%. *Joule* **3**, 177–190 (2019).
26. Bu, T. *et al.* Lead halide-templated crystallization of methylamine-free perovskite for efficient photovoltaic modules. *Science* **372**, 1327–1332 (2021).
27. Lin, Y. H. *et al.* A piperidinium salt stabilizes efficient metal-halide perovskite solar cells. *Science* **369**, 96–102 (2020).
28. Qin, M. *et al.* Precise control of perovskite crystallization kinetics via sequential A-site doping. *Adv. Mater.* **32**, e2004630 (2020).
29. Lee, J. W. *et al.* Control of crystal growth toward scalable fabrication of perovskite solar cells. *Adv. Funct. Mater.* **29**, 1807047 (2018).
30. Wang, R. *et al.* Constructive molecular configurations for surface-defect passivation of perovskite photovoltaics. *Science* **366**, 1509–1513 (2019).
31. Chen, C. H. *et al.* Ternary two-step sequential deposition induced perovskite orientational crystallization for high-performance photovoltaic devices. *Adv. Energy Mater.* **11**, 2101538 (2021).

32. Liu, Y. W. *et al.* Flexible lead bromide perovskite solar cells. *ACS Appl. Energy Mater.* **3**, 9817–9823 (2020).
33. Hu, X. T. *et al.* A mechanically robust conducting polymer network electrode for efficient flexible perovskite solar cells. *Joule* **3**, 2205–2218 (2019).
34. Ren, N. Y. *et al.* Humidity-resistant flexible perovskite solar cells with over 20% efficiency. *Solar RRL* **5**, 2000795 (2021).
35. Yang, D. *et al.* High efficiency flexible perovskite solar cells using superior low temperature TiO₂. *Energy Environ. Sci.* **8**, 3208–3214 (2015).
36. Bi, C. *et al.* Efficient flexible solar cell based on composition-tailored hybrid perovskite. *Adv. Mater.* **29**, (2017).
37. Palmstrom, A. F. *et al.* Enabling flexible all-perovskite tandem solar cells. *Joule* **3**, 2193–2204 (2019).
38. Zhong, M. Y. *et al.* Highly efficient flexible MAPbI₃ solar cells with a fullerene derivative-modified SnO₂ layer as the electron transport layer. *J. Mater. Chem. A* **7**, 6659–6664 (2019).
39. Yang, J. *et al.* High-performance perovskite solar cells with excellent humidity and thermo-stability via fluorinated perylenediimide. *Adv. Energy Mater.* **9**, 1900198 (2019).
40. Li, M. *et al.* Perovskite grains embraced in a soft fullerene network make highly efficient flexible solar cells with superior mechanical stability. *Adv. Mater.* **31**, e1901519 (2019).
41. Duan, X. *et al.* Controlling crystal growth via an autonomously longitudinal scaffold for planar perovskite solar cells. *Adv. Mater.* **32**, e2000617 (2020).
42. Al-Ashouri, A. *et al.* Monolithic perovskite/silicon tandem solar cell with >29% efficiency by enhanced hole extraction. *Science* **370**, 1300–1309 (2020).
43. Kim, D. *et al.* Efficient, stable silicon tandem cells enabled by anion-engineered wide-bandgap perovskites. *Science* **368**, 155–160 (2020).
44. Chen, B. B. *et al.* Insights into the development of monolithic perovskite/ silicon tandem solar cells. *Adv. Energy Mater.* 2003628 (2021).
45. Li, H. *et al.* *Perovskite tandem solar cells: from fundamentals to commercial deployment.* *Chem. Rev.* **120**, 9835–9950 (2020).
46. Hou, Y. *et al.* Efficient tandem solar cells with solution-processed perovskite on textured crystalline silicon. *Science* **367**, 1135–1140 (2020).
47. Bastiani, M. D. *et al.* Efficient bifacial monolithic perovskite/silicon tandem solar cells via bandgap engineering. *Nat. Energy* **6**, 167–175 (2021).
48. Isikgor, F. H. *et al.* Concurrent cationic and anionic perovskite defect passivation enables 27.4% perovskite/ silicon tandems with suppression of halide segregation. *Joule* **5**, 1566–1586 (2021).
49. Meng, K. *et al.* In situ observation of crystallization dynamics and grain orientation in sequential deposition of metal halide perovskites. *Adv. Funct. Mater.* **29**, 1902319 (2019).
50. Yang, X. *et al.* Superior carrier lifetimes exceeding 6 μs in polycrystalline halide perovskites. *Adv. Mater.* **32**, e2002585 (2020).

51. McKenna, K. P. Electronic properties of {111} twin boundaries in a mixed-ion lead halide perovskite solar absorber. *ACS Energy Lett.* **3**, 2663–2668 (2018).
52. Hou, F. H, *et al.* Inverted pyramidally-textured PDMS antireflective foils for perovskite/silicon tandem solar cells with flat top cell. *Nano Energy* **56**, 234–240 (2019).
53. Saidaminov, M. I. *et al.* Suppression of atomic vacancies via incorporation of isovalent small ions to increase the stability of halide perovskite solar cells in ambient air. *Nat. Energy* **3**, 648–654 (2018).
54. Blöchl, P. E. *et al.* Projector augmented-wave method. *Phys. Rev. B* **50**, 17953 (1994).
55. Kresse, G. *et al.* From ultrasoft pseudopotentials to the projector augmented-wave method. *Phys. Rev. B* **59**, 1758 (1999).
56. Kresse, G. *et al.* Efficiency of ab-initio total energy calculations for metals and semiconductors using a plane-wave basis set. *Comp. Mater. Sci.* **6**, 15–50 (1996).
57. Kresse, G. Furthmüller, J. Efficient iterative schemes for ab initio total-energy calculations using a plane-wave basis set. *Phys. Rev. B* **54**, 11169 (1996).
58. Perdew, J. P. Burke, K. Ernzerhof, M. Generalized gradient approximation made simple. *Phys. Rev. Lett.* **77**, 3865 (1996).
59. Grimme, S. *et al.* Semiempirical GGA-type density functional constructed with a long-range dispersion correction. *J. Comp. Chem.* **27**, 1787–1799 (2006).
60. Flahaut, E. *et al.* Crystallization of 2H and 4H PbI₂ in carbon nanotubes of varying diameters and morphologies. *Chem. Mater.* **18**, 2059–2069 (2006).

Table

Table 1. Parameters of champion devices based on Control and CdAc₂ perovskite thin films.

Names	VOC (V)	J _{SC} (mA/cm ²)	FF (%)	PCE (%)
Flexible substrate-Control	1.096	24.32	74.48	19.86
Flexible substrate-CdAc ₂	1.167	24.63	79.27	22.78
Rigid substrate-CdAc ₂	1.169	25.75	81.24	24.46

Figures

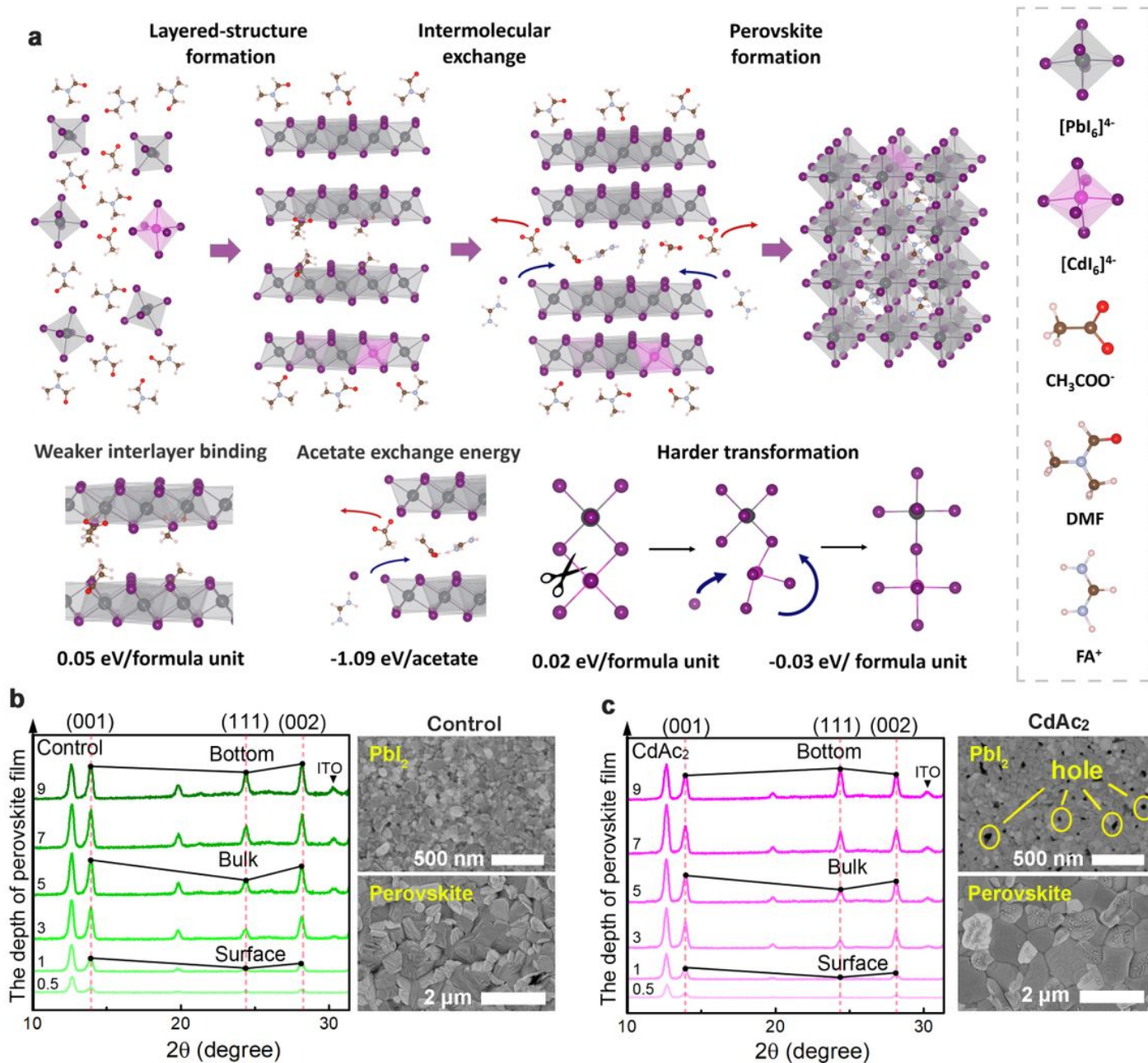


Figure 1

Schematic formation of nano-hole array PbI₂ and FAPbI₃ films. (a) Illustration of thin-film growth mechanism for the perovskite with and without the addition of CdAc₂. (b) and (c) GIXRD of perovskite films without and with CdAc₂, the angles varied from 0.5° to 9° (inset image: surface-sectional SEM images of PbI₂ films and perovskite films).

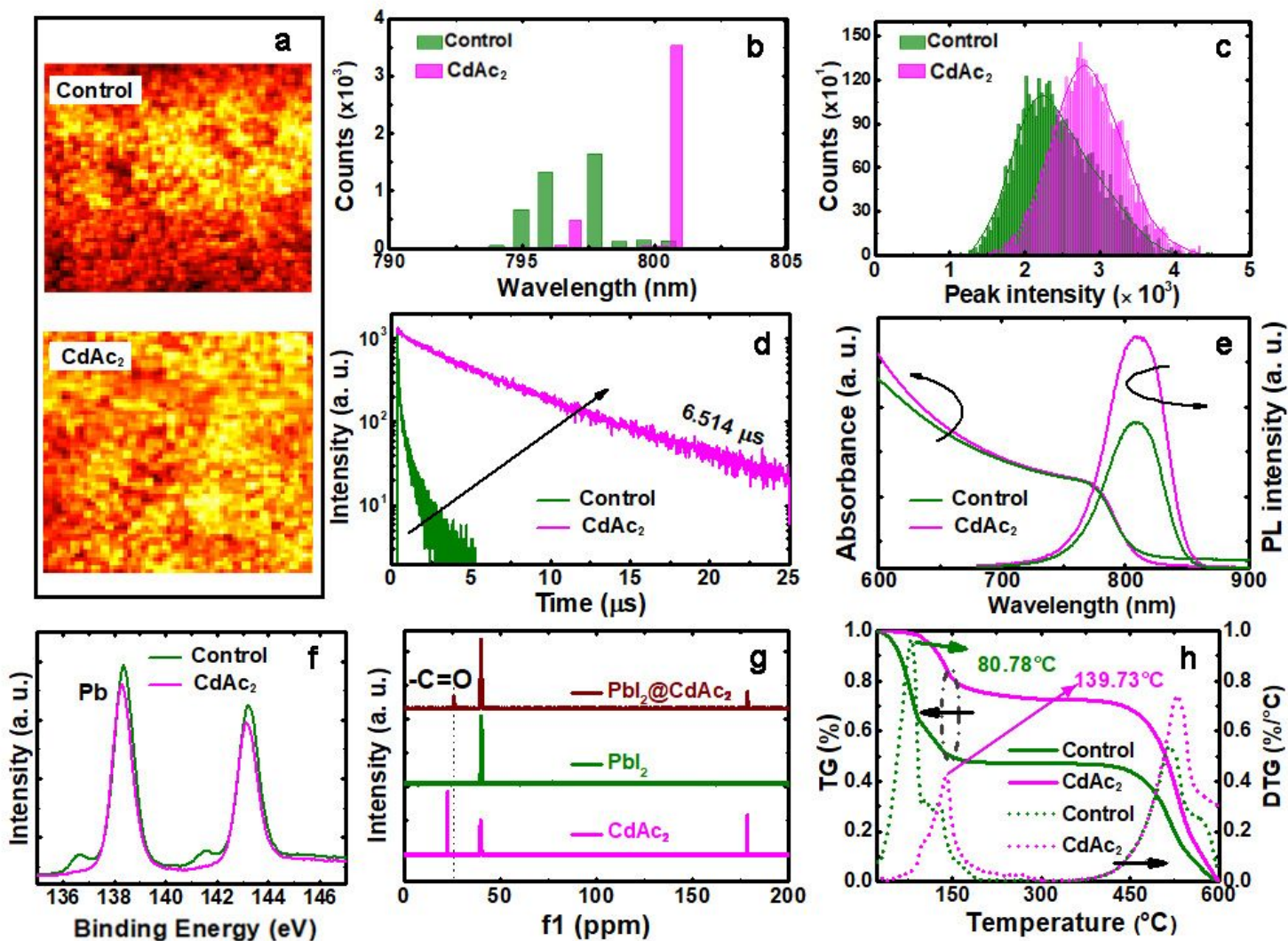


Figure 2

Characterization of the FAPbI₃ films on flexible PET/ITO substrates. The photoluminescence (PL) (a) mapping and (b) peak position of perovskite films prepared with or without CdAc₂ (region size: 20 x 20 mm). (c) Histograms of PL peak position (extracted from PL mapping data) of perovskite films prepared with or without CdAc₂. (d) Time-resolved photoluminescence of the FAPbI₃ films. (e) UV-vis absorption and PL spectra of the FAPbI₃ films. (f) XPS core-level spectra of Pb on perovskite films prepared with or without CdAc₂. (g) ¹³C solution-state NMR spectra of Precursor PbI₂ solution. (h) TGA curve of precursor PbI₂ solution with and without CdAc₂.

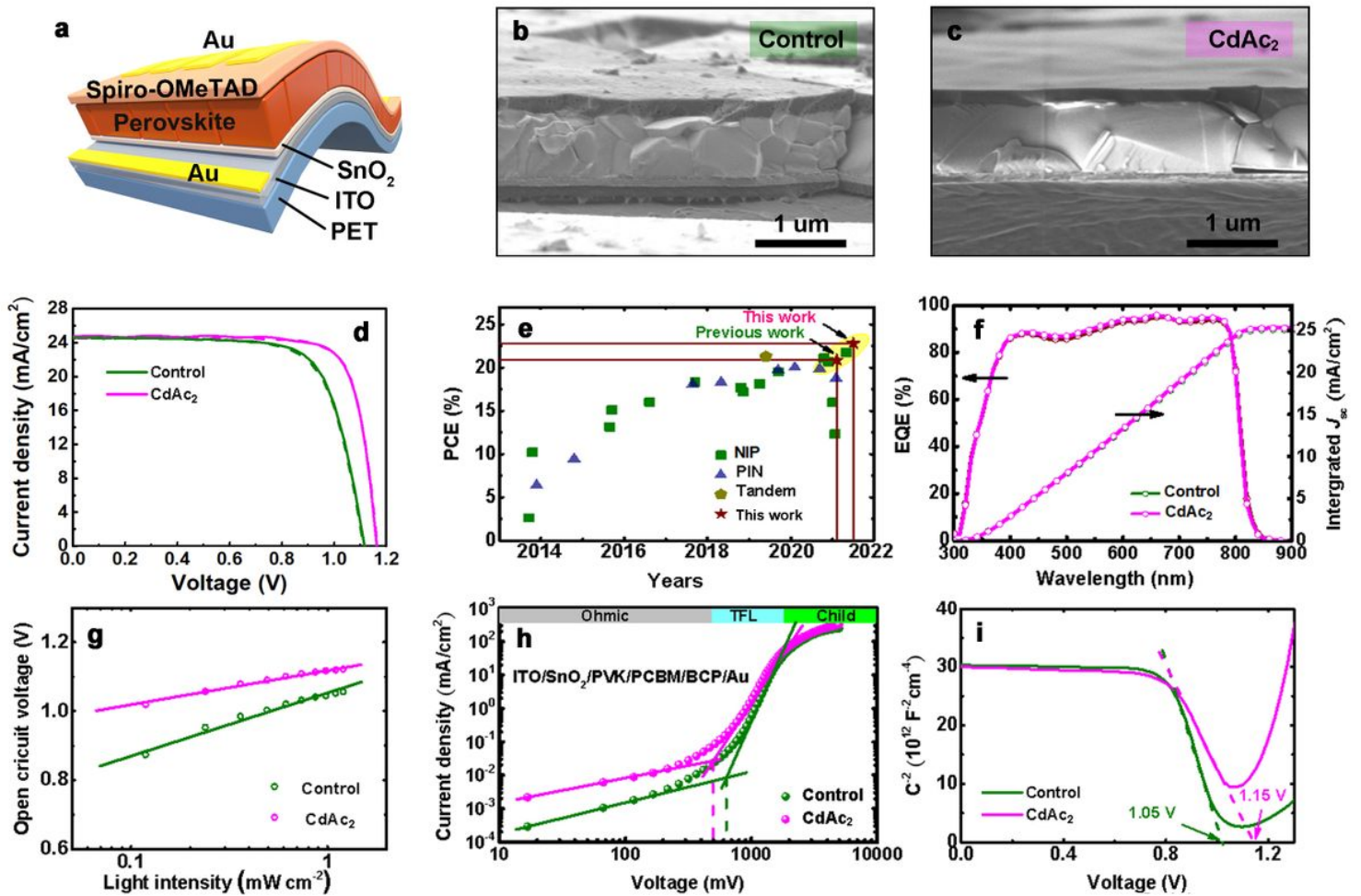


Figure 3

Characterization of the photovoltaic performance and stability of FPSCs. (a) The configuration of typical flexible perovskite solar cells adopted in this work. Cross-section images of control (b) and CdAc₂ treated (c) FPSCs. (d) J–V curves and (e) Efficiency evolution of FPSCs. (f) EQE of the control and CdAc₂ treated FPSCs. (g) The relationship between the V_{OC} and light intensity for the control and CdAc₂ treated FPSCs. (h) Space-charge-limited current (SCLC) model with a device structure of ITO/ETL/Perovskite/PCBM/Cu. (i) Mott-Schottky measurement for control and CdAc₂ treated FPSCs.

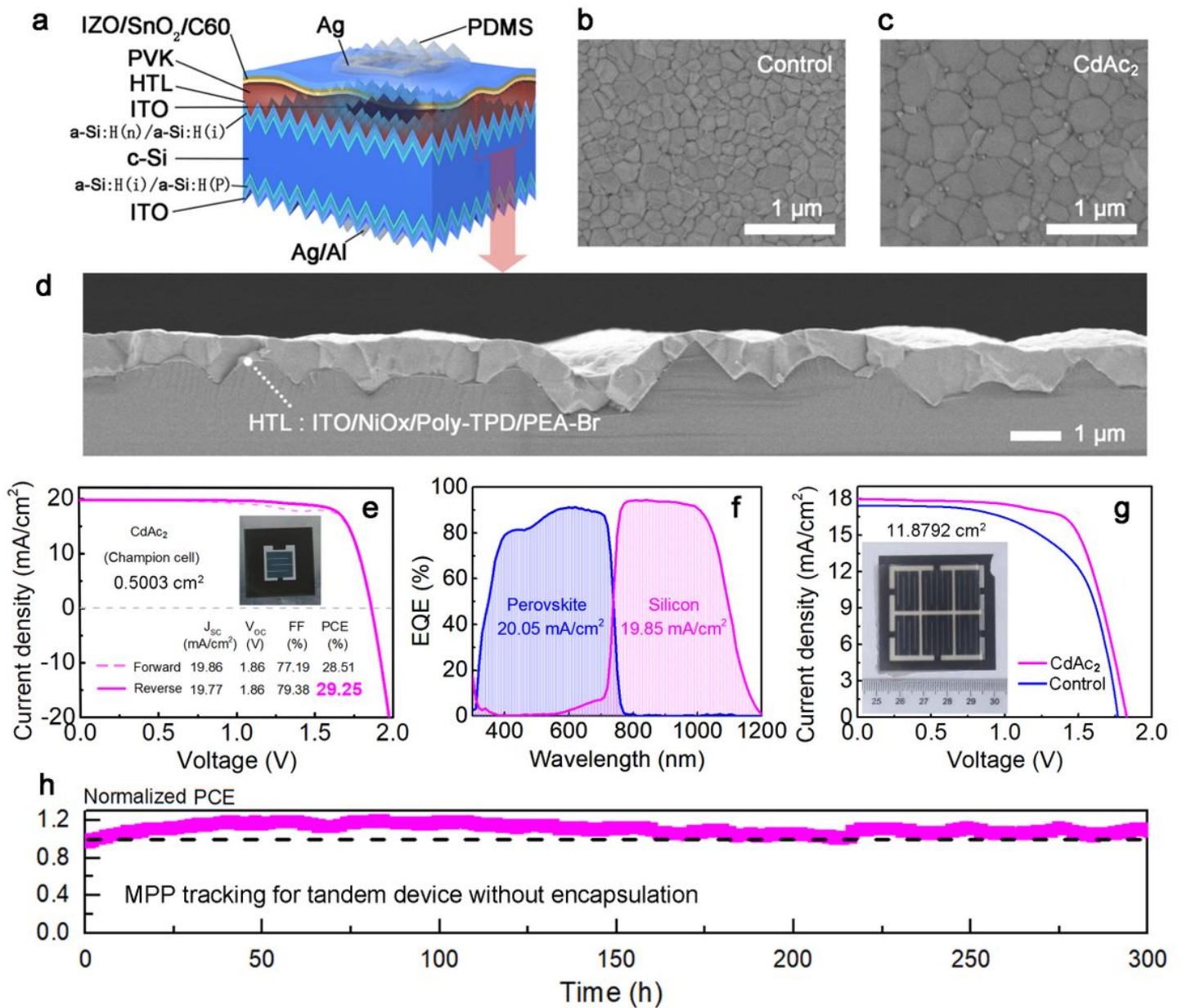


Figure 4

Characteristics of monolithic perovskite/silicon tandem solar cells based on textured substrate using CdAc₂. (a) Schematic stack of the monolithic perovskite/silicon tandem solar cell. SEM top-view image of solution-processed perovskite film without (b) and with (b) CdAc₂. (d) SEM cross-section image of a textured c-Si with an average pyramid size of 2 μm (e) *J-V* characteristics of tandem solar cells without and with CdAc₂ with an effective area of 0.5003 cm². The illustration is the photo of a complete tandem device. (f) The EQE of the tandem device with CdAc₂ treatment. (g) *J-V* characteristics of tandem solar cells without and with CdAc₂ with an effective area of 11.8792 cm². The illustration is a photo of a complete tandem device. (h) Mpp tracking for TSCs without encapsulation.

Supplementary Files

This is a list of supplementary files associated with this preprint. Click to download.

- [CCDSIsubmit.docx](#)